Electronic Supplementary Material (ESI) for Materials Chemistry Frontiers.

Supporting Information

Rational design of efficient counter electrode with $Co/Co_1P_1N_3$ atomic interface for promoting catalytic performance

Danni Zhou, ‡[a] Zhaoming Xia, ‡[b] Huishan Shang, ‡[c] Hai Xiao,[b] Zhuoli Jiang,[b] Haijing Li,[d] Lirong Zheng,[d] Juncai Dong,[d] and Wenxing Chen*[a]

[a.] Energy & Catalysis Center, School of Materials Science and Engineering, Beijing Institute of Technology, Beijing 100081, China. E-mail: wxchen@bit.edu.cn.

[b.]Department of Chemistry, Tsinghua University, Beijing, 100084, P. R. China.

[c.]School of Chemical Engineering, Zhengzhou University, Zhengzhou 450001, P. R. China

[d.]Beijing Synchrontron Radiation Facility, Institute of High Energy Physics, Chinese Academy of Science, Beijing 100029, China

* Corresponding author. E-mail: wxchen@bit.edu.cn.

‡ These authors contributed equally to this work.

Table of contents

Section1: Experiment Section

Materials

Cobalt nitrate hexahydrate (98%, Alfa), 2-methylimidazole (Acros), triphenylphosphine (PPh_3, 99.5%, Alfa), methanol (Sinopharm Chemical) were used without any further purification. Ultrapure water (Millipore Milli-Q grade) with a resistivity of 18.2 MΩ was used in all the experiments.

Synthesis of Samples

Synthesis of $Co/Co_1P_1N_3$: The 2-methylimidazole (0.616g) was firstly dissolved in 15 ml methanol with well stirring (solution Ⅰ). Second, $Co(NO_3)_2·6H_2O$ (0.546 g), and PPh_3 (0.375 g) were dissolved in 30 ml methanol with stirring to prepare well dissolving solution Ⅱ. Then, solution Ⅰ was quickly added into solution Ⅱ with strong stirring for 0.5 h at room temperature. Next, the mixture solution was transferred into a 100 ml Teflon-lined stainless-steel autoclave and heated at 120 °C for 4 h. The as-prepared products were collected by centrifugation process and washed with methanol for three times. Finally, they were dried at 70 °C under vacuum condition for 12 h. The obtained powders were calcined at 900 °C for 3h under nitrogen gas and then cooled to room temperature. The $Co/Co_1P_1N_3$ was collected without further treatment.

Synthesis of Co/Co_1N_4： The 2-methylimidazole (0.616g) was firstly dissolved in 15 ml methanol with well stirring (solution Ⅰ). Second, $Co(NO_3)_2·6H_2O$ (0.546g) was dissolved in 30 ml methanol with stirring to prepare well dissolving solution Ⅱ. Then, solution Ⅰ was quickly added into solution Ⅱ with strong stirring for 0.5 h at room temperature. Next, the mixture solution was transferred into a 100 ml Teflon-lined stainless-steel autoclave and heated at 120 °C for 4h. The as-prepared products were collected by centrifugation process and washed with methanol for three times. Finally, they were dried at 70 °C under vacuum condition for 12 h. The obtained powders were calcined at 900 °C for 3h under nitrogen gas and then cooled to room temperature. The Co/Co_1N_4 was collected without further treatment.

Synthesis of PNC： The 2-methylimidazole (0.616g) was firstly dissolved in 15 ml methanol with well stirring (solution Ⅰ). Second, $Zn(NO_3)_2·6H_2O$ (0.558g) and PPh_3 (0.375g) were dissolved in 30 ml methanol with stirring to prepare well dissolving solution Ⅱ. Then, solution Ⅰ was quickly

added into solution Ⅱ with strong stirring for 0.5 h at room temperature. Next, the mixture solution was transferred into a 100 ml Teflon-lined stainless-steel autoclave and heated at 120 °C for 4h. The as-prepared products were collected by centrifugation process and washed with methanol for three times. Finally, they were dried at 70 °C under vacuum condition for 12 h. The obtained powders were calcined at 1000 °C for 3h under nitrogen gas and then cooled to room temperature. The PNC matrix was collected without further treatment.

Synthesis of NC： The 2-methylimidazole (0.616g) was firstly dissolved in 15 ml methanol with well stirring (solution Ⅰ). Second, $Zn(NO_3)_2 \cdot 6H_2O$ (0.558g), were dissolved in 30 ml methanol with stirring to prepare well dissolving solution Ⅱ. Then, solution Ⅰ was quickly added into solution Ⅱ with strong stirring for 0.5 h at room temperature. Next, the mixture solution was transferred into a 100 ml Teflon-lined stainless-steel autoclave and heated at 120 °C for 4h. The as-prepared products were collected by centrifugation process and washed with methanol for three times. Finally, they were dried at 70 °C under vacuum condition for 12 h. The obtained powders were calcined at 1000 °C for 3h under nitrogen gas and then cooled to room temperature. The NC matrix was collected without further treatment.

Characterization

The composition and structure of the as-prepared products were characterized by powder X-ray diffraction (XRD, RigakuTTR-III X-ray diffractometer with Cu Kα radiation, λ=1.5418Å). The morphologies were observed by a scanning electron microscope (SEM, JSM-6700F, 5kV) and a transmission electron microscope (TEM, JEOL JEM-2100F microscope, 200kV). The HAADF-STEM images and EDS elemental mapping were carried out in a JEOL ARM-200 microscope at 200 kV, equipped with a probe spherical aberration corrector. The samples were dispersed in ethanol and dropped onto a copper grid with a carbon film coated for TEM characterizations.

***Ex-situ* XAFS measurements**

The X-ray absorption find structure spectra data were collected at BL14W1 station in Shanghai Synchrotron Radiation Facility (SSRF, operated at 3.5 GeV with a maximum current of 250 mA), respectively. The data were collected at room temperature (Co K-edge in fluorescence excitation mode using a 7 element Ge detector). All samples were pelletized as disks of 13 mm diameter with 1mm thickness using graphite powder as a binder (XAFS data processing).

***In-situ* XAFS measurements**

A catalyst modified carbon paper was used as working electrode, graphite rod as counter electrode and Ag/AgCl (KCl-saturated) electrode as reference electrode. A home-made electrochemical cell was used for *in-situ* XAFS measurements. The experiments were performed at BL1W1B station in BSRF.

XAFS data processing

The acquired EXAFS data were processed according to the standard procedures using the Athena and Artemis implemented in the IFEFFIT software packages. The fitting detail is described below:

The acquired EXAFS data were processed according to the standard procedures using the ATHENA module implemented in the IFEFFIT software packages. The EXAFS spectra were obtained by subtracting the post-edge background from the overall absorption and then normalizing with respect to the edge-jump step. Subsequently, the χ(k) data of were Fourier transformed to real (R) space using a hanning windows (dk=1.0 $Å^{-1}$) to separate the EXAFS contributions from different coordination shells. To obtain the quantitative structural parameters around central atoms, least-squares curve parameter fitting was performed using the ARTEMIS module of IFEFFIT software packages.[11]

The following EXAFS equation was used:

$$\chi(k)=\sum_j \frac{N_j S_o^2 F_j(k)}{k R_j^2}\exp[-2k^2\sigma_j^2]\exp[\frac{-2R_j}{\lambda(k)}]\sin[2kR_j+\phi_j(k)] \quad \text{(S1)}$$

S_0^2 is the amplitude reduction factor, $F_j(k)$ is the effective curved-wave backscattering amplitude, N_j is the number of neighbors in the j^{th} atomic shell, R_j is the distance between the X-ray absorbing central atom and the atoms in the j^{th} atomic shell (backscatterer), λ is the mean free path in Å, $\phi_j(k)$ is the phase shift (including the phase shift for each shell and the total central atom phase shift), σ_j is the Debye-Waller parameter of the j^{th} atomic shell (variation of distances around the average R_j). The functions $F_j(k)$, λ and $\phi_j(k)$ were calculated with the ab initio code FEFF8.2. The additional details for EXAFS simulations are given below.

The coordination numbers of model samples were fixed as the nominal values. The obtained S_0^2 was fixed in the subsequent fitting. While the internal atomic distances R, Debye-Waller factor σ^2, and the edge-energy shift ΔE_0 were allowed to run freely.

Device fabrication

FTO-coated glass substrates were cleaned by ultrasonication with acetone, ethanol and deionized water, and subjected to an O_3 treatment for 30 min. A 20-nm-thick TiO_2 compact layer was then deposited on the substrates by spin-coating method and sintered at 450 °C for 30 min in a muffle-type furnace. Subsequently, a 10-μm-thick mesoporous TiO_2 layer composed of 20 nm nanopartciles and a 5-μm-thick light scattering TiO_2 layer composed of 400 nm nanoparticles were successively deposited by doctor blade method, and sintered under 450 °C for 30 min. A post treatment of the sintered TiO_2 film with an aqueous solution of $TiCl_4$ (0.04 M) was then carried out for 30 min at 70 °C. Afterward, the treated photoanodes were sensitized with 0.5 mM N719 (commercial ruthenium-based molecule dye) in ethanol solution at room temperature for 12 hours. The DSSCs were assembled by sandwiching the sensitized photoanodes and $Co/Co_1P_1N_3$, Co/Co_1N_4, PNC, NC, and Pt counter electrodes, with 100 μm thick adhesive tapes as spacer. The redox electrolyte was consisted of 1 M PMII (1-methyl-3-propyl imidazolium iodide), 0.04 M LiI, 0.03 M I_2, 0.1 M GuSCN (guanidinium thiocyanate), 0.5 M TBP (4-tert-butylpyridine) in acetonitrile and propylene carbonate (v/v = 1:1). The $Co/Co_1P_1N_3$ and other counter electrodes (CEs) were fabricated by spin-coating technique (~2.5 mg/mL in ethanol).

Electrochemical measurements

Cyclic voltammetry (CV) and electrochemical impedance spectroscopy (EIS) were carried out with an electrochemical workstation (CHI-660). CV curves were recorded at a scan rate of 50 mV/s in acetonitrile solution containing 10 mM LiI and 1 mM I_2 in a conventional three electrodes system, in which various catalysts, Pt sheet and Ag/AgCl were used as working electrode, counter electrode and reference electrode, respectively. EIS were measured with a symmetrical dummy CE-CE cell. The identical CEs were separated by the adhesive tapes of 100 μm in thickness. EIS was performed with the frequency ranging from 100 KHz to 0.1 Hz at zero bias potential and the amplitude of the AC signal was 10 mV. We used the Zview modeling software to fit the data according to equivalent circuit derived from transmission line model.

Photocurrent-voltage (*J-V*) curves were measured by a Keithley digital source meter (Keithley 2420, USA) under AM 1.5, 100 mW cm^{-2} irradiation (Newport Oriel Solar Simulator, Model 91159A). Prior to *J-V* measurement, the light intensity was calibrated with a NREL certified standard crystalline silicon solar cell (4 cm^2). The active area of the cells was set to 0.25 cm^2.

DFT parameters

Density functional theory (DFT) calculations with plane-wave basis set were performed using the projector augmented wave (PAW) methods[1] by the Vienna Ab initio Simulation Package (VASP)[2-5] with the generalized gradient approximation (GGA) based on the Perdew−Burke−Ernzerhof (PBE)[6] exchange-correlation functional. A Gamma centered Monkhorst-Pack grids of 1 x 1x 1 was sampled for the Brillouin zone. The plane-wave cutoff energy of 400 was employed. All calculations were performed with spin polarization. The simulated unit cells are constructed with one layer of (5×5) supercells of graphene and three layers of (5×5) supercells of fcc Co (111). A vacuum layer of 15 Å was added for the surface slabs along the z-direction. In the geometric optimization, all atoms were allowed to relax until the calculated Hellmann-Feynman forces smaller than 0.03 eV/Å.

IRR can be generally described as follows reactions:

$$I_3^-(sol) \rightleftharpoons I_2(sol) + I^-(sol) \quad (S2)$$

$$I_2(sol) + * + e^- \rightleftharpoons *I + I^-(sol) \quad (S3)$$

$$*I + e^- \rightleftharpoons *+ I^-(sol) \quad (S4)$$

where the process eq. (S2) was generally much faster than process eq. (S3) and eq. (S4). Thus, process eq. (S3) and eq. (S4) determined the reaction rate of the whole reduction reaction and influent the overall electrocatalytic activity. Therefore, to simplify the calculation process, only process eq. (S3) and eq. (S4) were taken into consideration. The total reaction is shown as follows:

$$I_2(sol) + 2e^- \rightleftharpoons 2I^- \quad (S5)$$

The chemical potential of I_2(sol) and I^- were unknown. However, there is a dynamic dissolution equilibrium between I_2(sol) and I_2(g).

$$I_2(sol) \rightleftharpoons I_2(g) \quad \text{(S6)}$$

The reaction (S6) is also fast. Thus, the reaction rate of reaction (S5) approximately equals to the rate of the follow reaction:

$$I_2(g) + 2e^- \rightleftharpoons 2I^-(sol) \quad \text{(S7)}$$

It can be divided into 2 parts:

$$I_2(g) + * + e^- \rightleftharpoons *I + I^-(sol) \quad \text{(S8)}$$

$$*I + e^- \rightleftharpoons *+ I^-(sol) \quad \text{(S9)}$$

The standard electrode potential of reaction (S7) is $E_0 = 0.5355$ V (vs. SHE) in standard temperature and pressure. We assume a bias voltage of $U = E_0$ is applied so that the chemical potential of $2I^- - 2e^-$ equals to the chemical potential of $I_2(g)$. The adsorption energy and free energy of I is calculated by follow equation, respectively:

$$Ead = E_{cat+I} - E_{cat} - 0.5\, E_{I2} \quad \text{(S10)}$$

$$G = E + ZPE - TS \quad \text{(S11)}$$

$$\Delta G_I = G_{cat+I} - G_{cat} - 0.5\, G_{I2} \quad \text{(S12)}$$

Where *E*ad is the adsorption energy; E_{cat+I} is the energy of the catalyst with an I atom adsorbed on its surface; E_{cat} is the energy of the catalyst; E_{I2} is the energy of I_2; ΔG_I is the Gibs free energy change of the I adsorption process. G_{cat+I} is the Gibs free energy of the catalyst with an I atom adsorbed on it; G_{slab} is the Gibs free energy of the catalyst; G_{I2} is the Gibs free energy of I_2; G is the Gibs free energy; E is the total energy; ZPE is the zero point energy; T is temperature; S is the entropy.

Section2: Supporting figures and tables

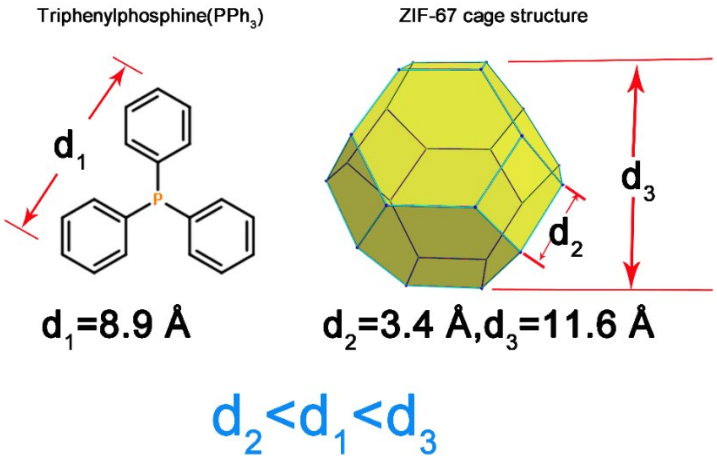

Fig. S1. Simulation results of size for triphenylphosphine (PPh_3) and ZIF-67 cage structure. The size of inner space within ZIF-67 cage can be suitable for PPh_3 molecular loading.

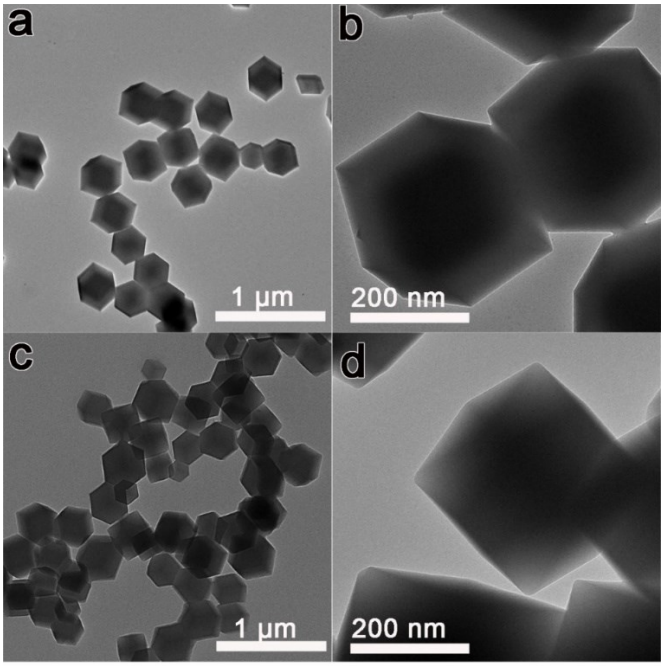

Fig. S2. TEM images of (a), (b) ZIF-67 and (c), (d) PPh_3@ZIF-67 at different magnification. TEM results displayed the uniform distribution of ZIF-67 and PPh_3@ZIF-67 nanoparticles.

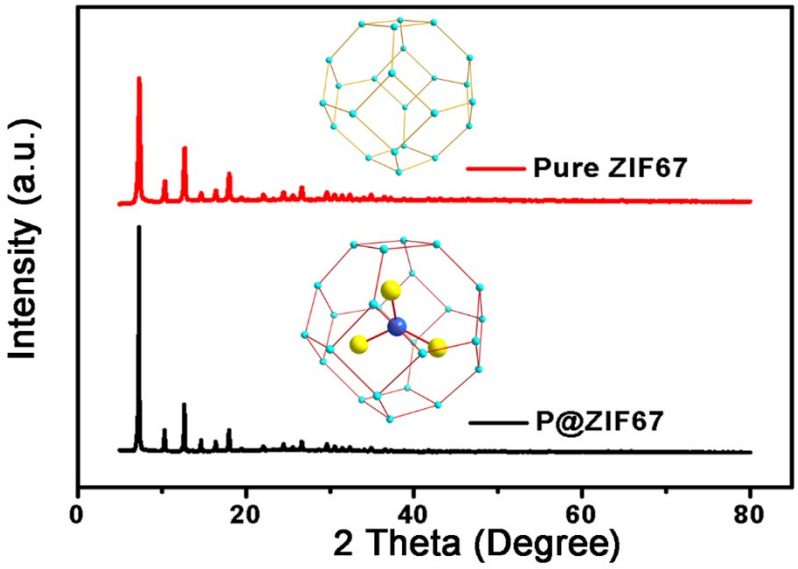

Fig. S3. XRD patterns of pure ZIF-67 and PPh_3@ZIF-67. XRD pattern of PPh_3@ZIF-67.

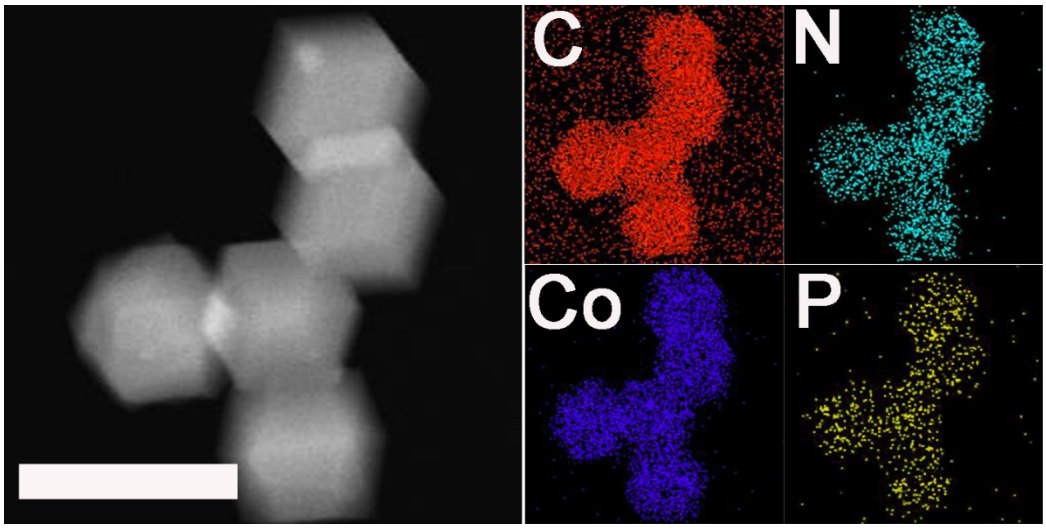

Fig. S4. Elemental mappings of PPh_3@ZIF-67.

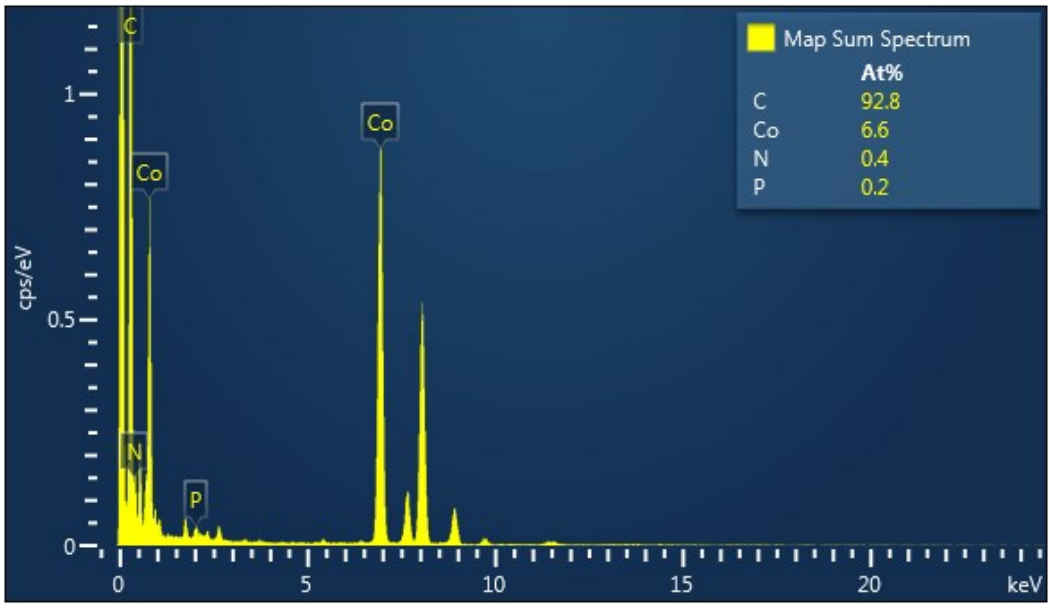

Fig. S5. EDS of $Co/Co_1P_1N_3$.

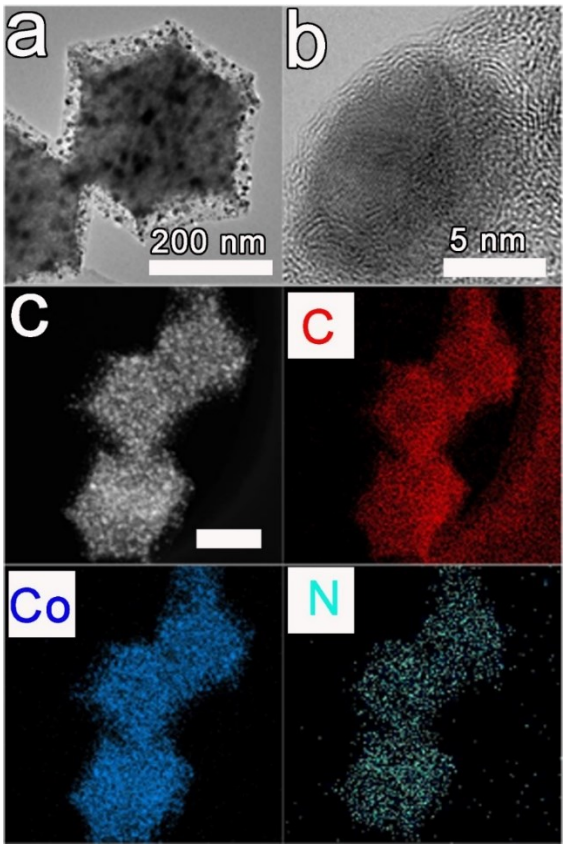

Fig. S6. Characterizations of **Co/Co_1N_4**: (a) TEM, (b) HRTEM, and (c) elemental mappings.

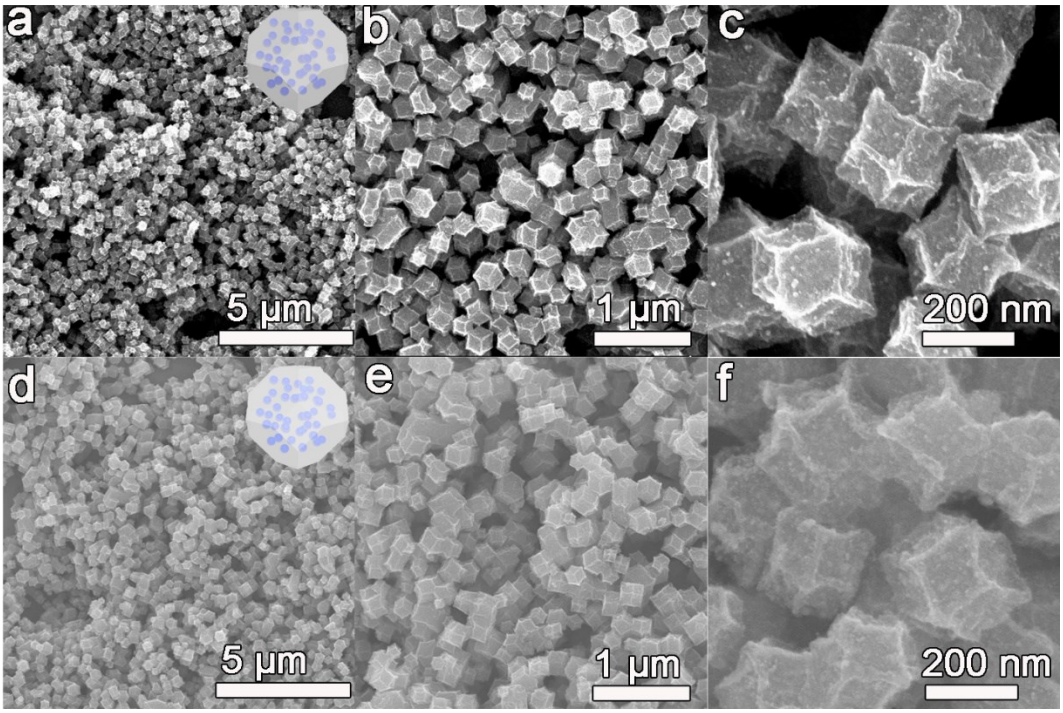

Fig. S7. (a-c) SEM images of $Co/Co_1P_1N_3$, (d-f) SEM images of Co/Co_1N_4.

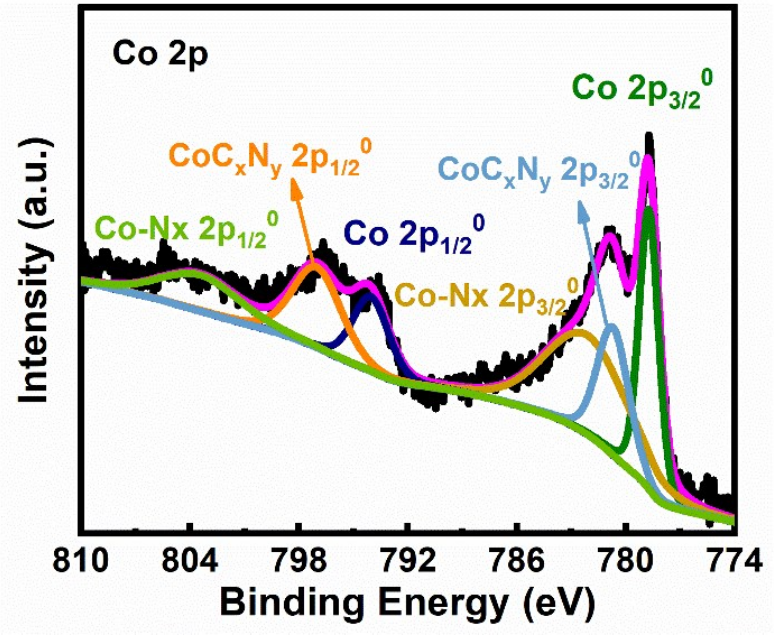

Fig. S8. Co 2p XPS results of $Co/Co_1P_1N_3$.

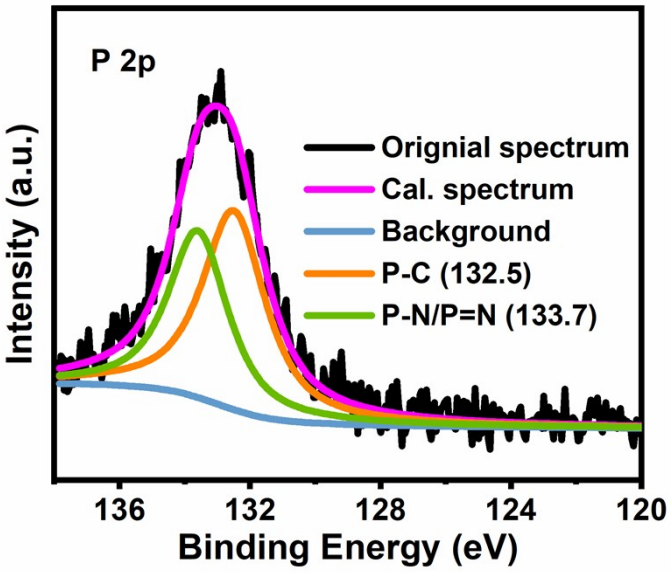

Fig. S9. P 2p XPS result of $Co/Co_1P_1N_3$ in situ. P 2p XPS possessed the peak at binding energy of 133.0 eV. This XPS peak can be fitted with two contributions located at 132.5 eV (P-C)[7] and 133.7 eV (P-N/P=N)[8-10]. P 2p XPS spectra exhibited both P-C and P-N/P=N in the as-prepared sample.

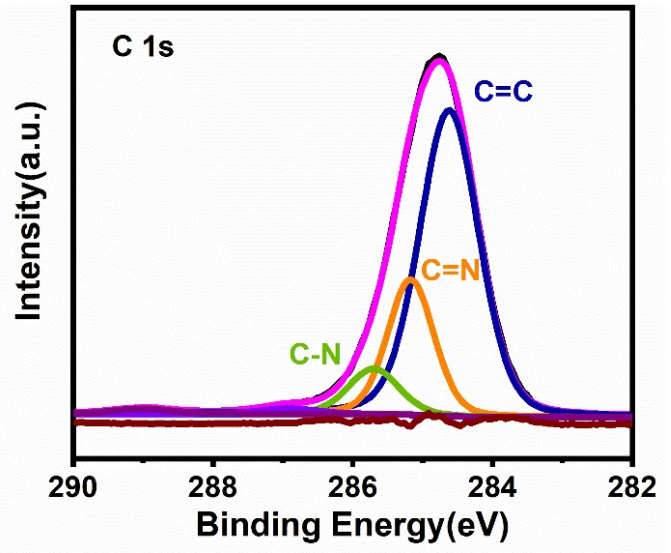

Fig. S10. C 1s XPS results of $Co/Co_1P_1N_3$. By XPS analysis, C=C, C-N, and C=N bonds can be recognized.

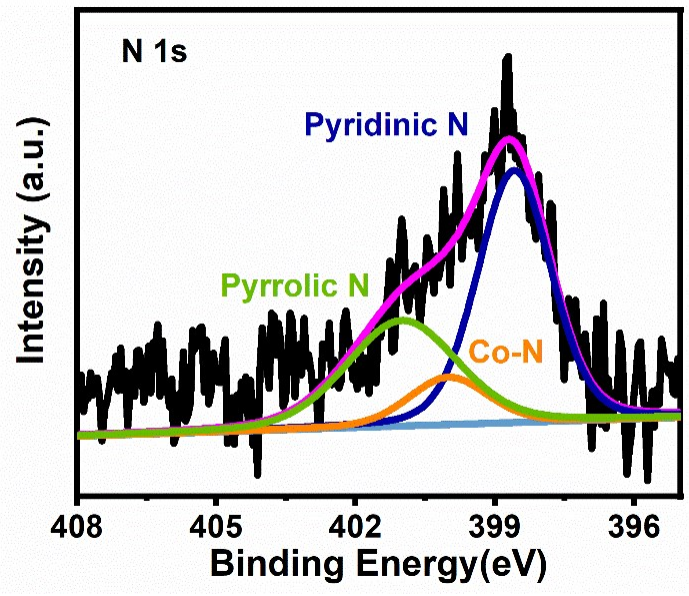

Fig. S11. N 1s XPS results of $Co/Co_1P_1N_3$. Pyridinic N, Pyrrolic N, Graphitic N and Co-N bond can be recognized.

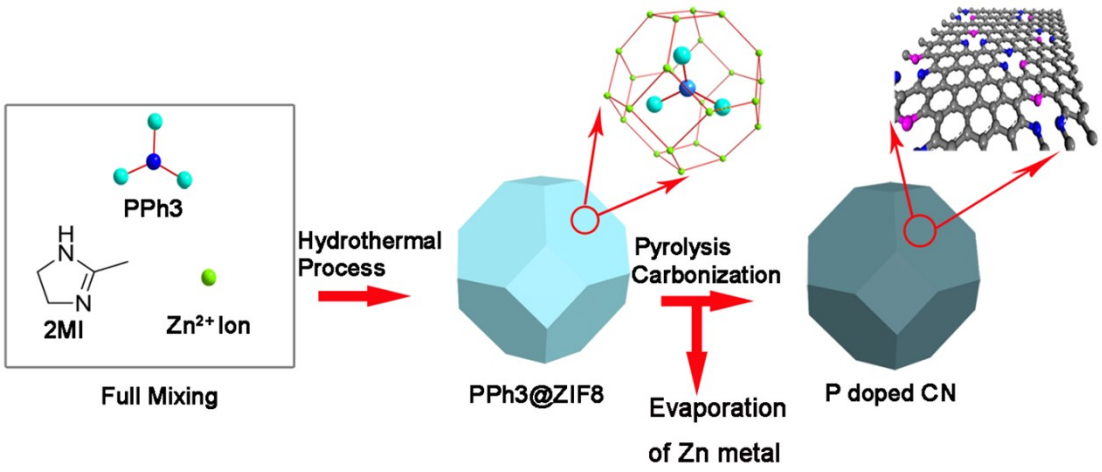

Fig. S12. Synthetic procedure of PNC.

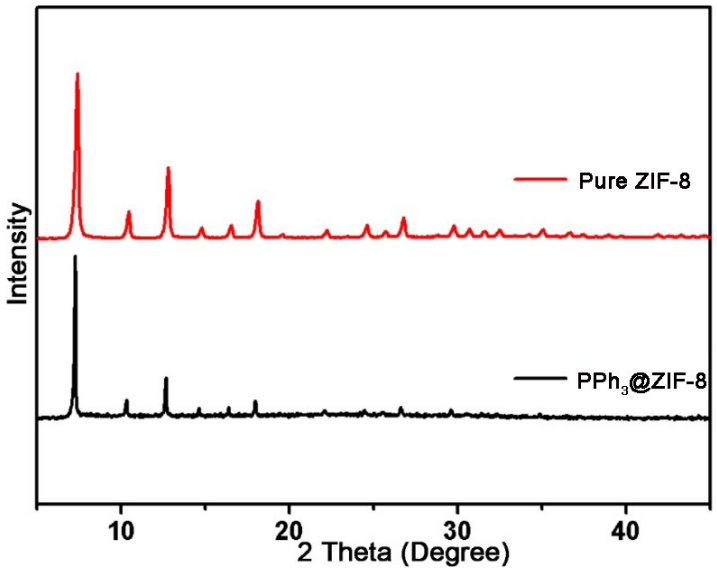

Fig. S13. XRD patterns of pure ZIF-8 and PPh_3@ZIF-8.

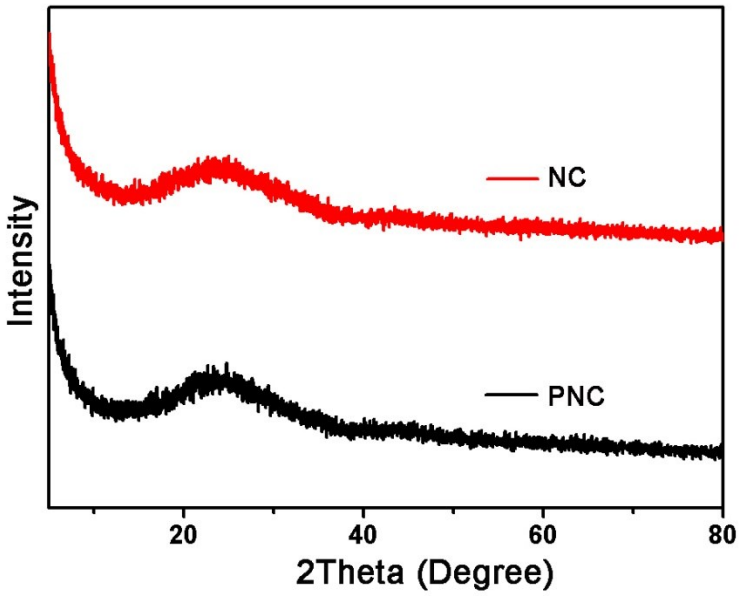

Fig. S14. XRD patterns of PNC and NC.

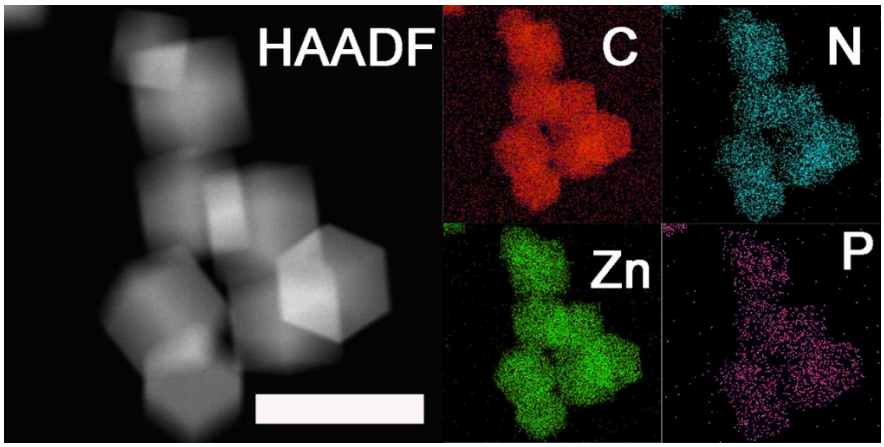

Fig. S15. Elemental mappings of PPh_3@ZIF-8.

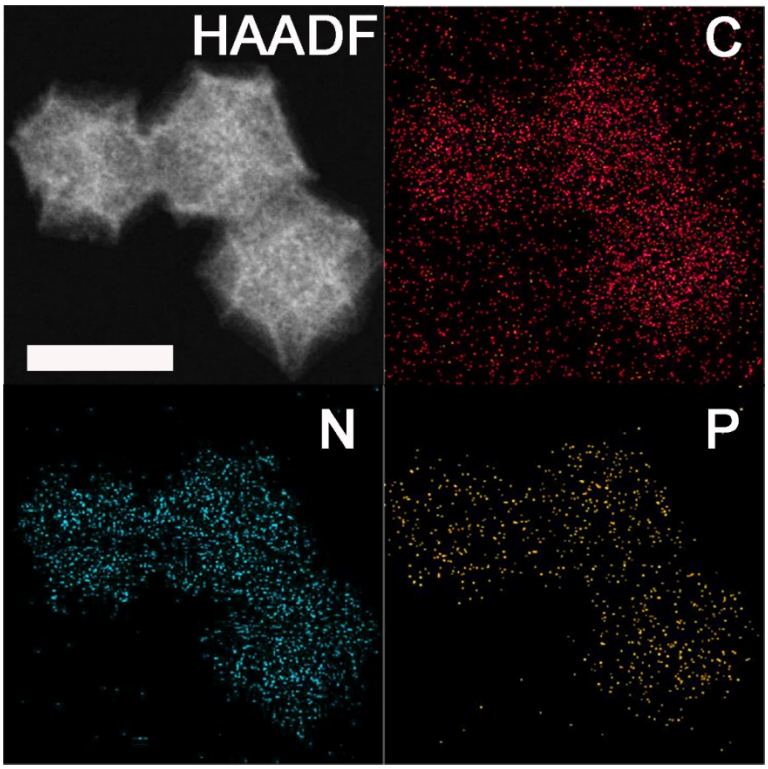

Fig. S16. Elemental mappings of PNC.

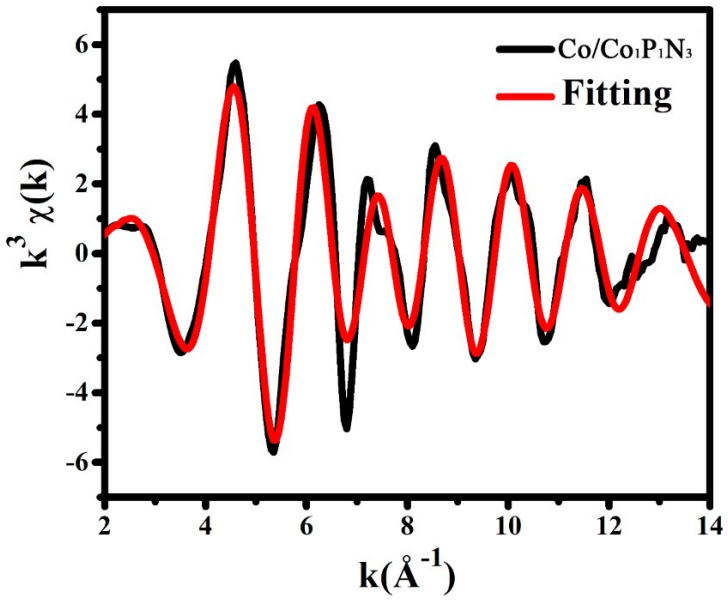

Fig. S17. The k space fitting curves of $Co/Co_1P_1N_3$ sample at Co K-edge.

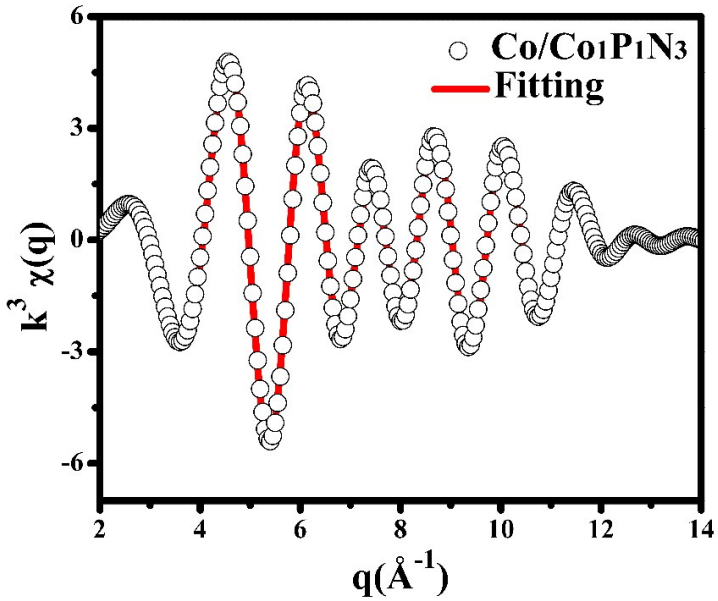

Fig. S18. The inversed FT-EXAFS fitting curves of $Co/Co_1P_1N_3$ sample at Co K-edge.

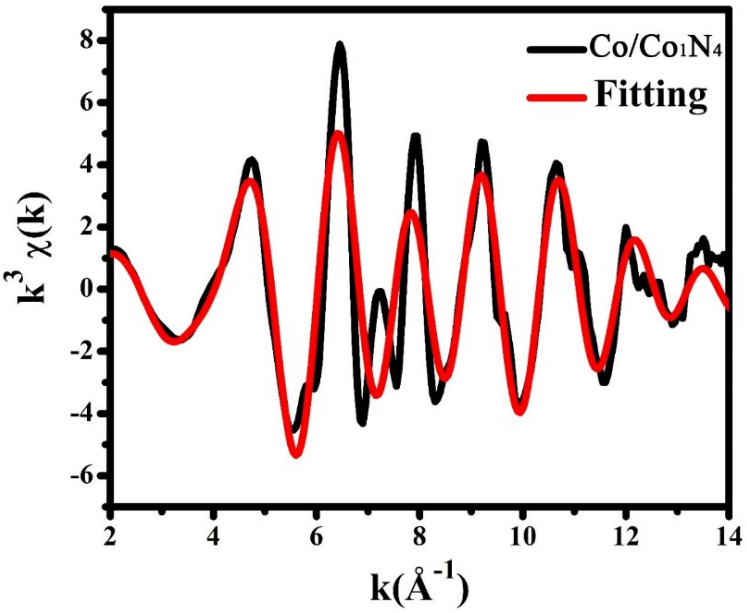

Fig. S19. The k space fitting curves of Co/Co_1N_4 sample at Co K-edge.

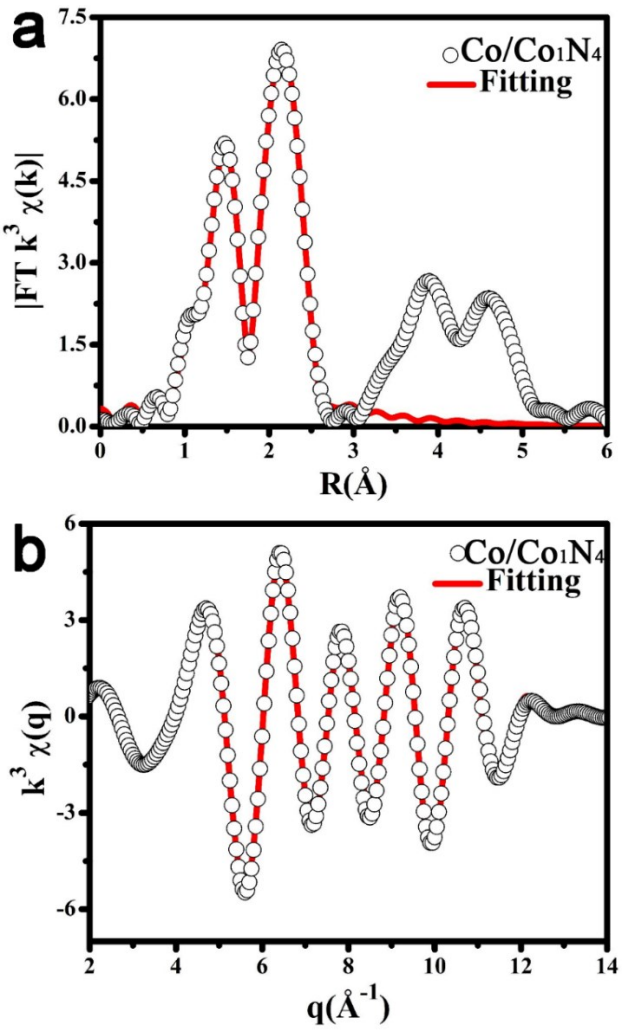

Fig. S20. (a) The FT-EXAFS fitting curves of Co/Co_1N_4 sample at Co K-edge. (FT range: 2-11.8 $Å^{-1}$; fitting range: 0.7-3.0 Å). (b) The inversed FT-EXAFS fitting curves of Co/Co_1N_4 sample at Co K-edge.

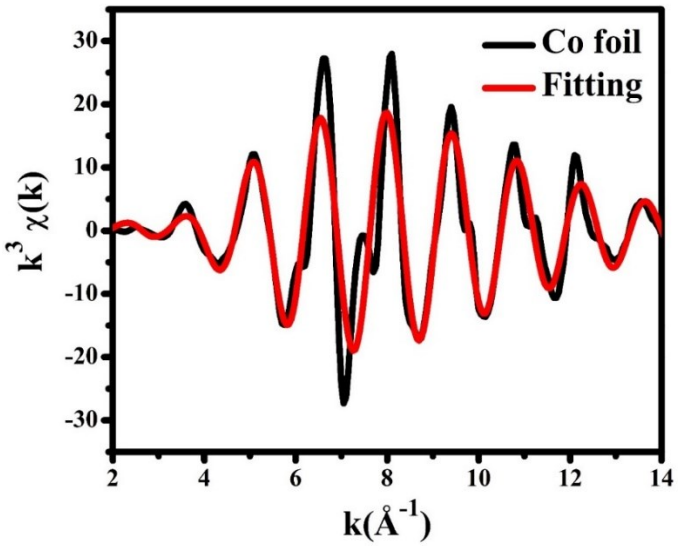

Fig. S21. The k space fitting curves of Co foil at Co K-edge.

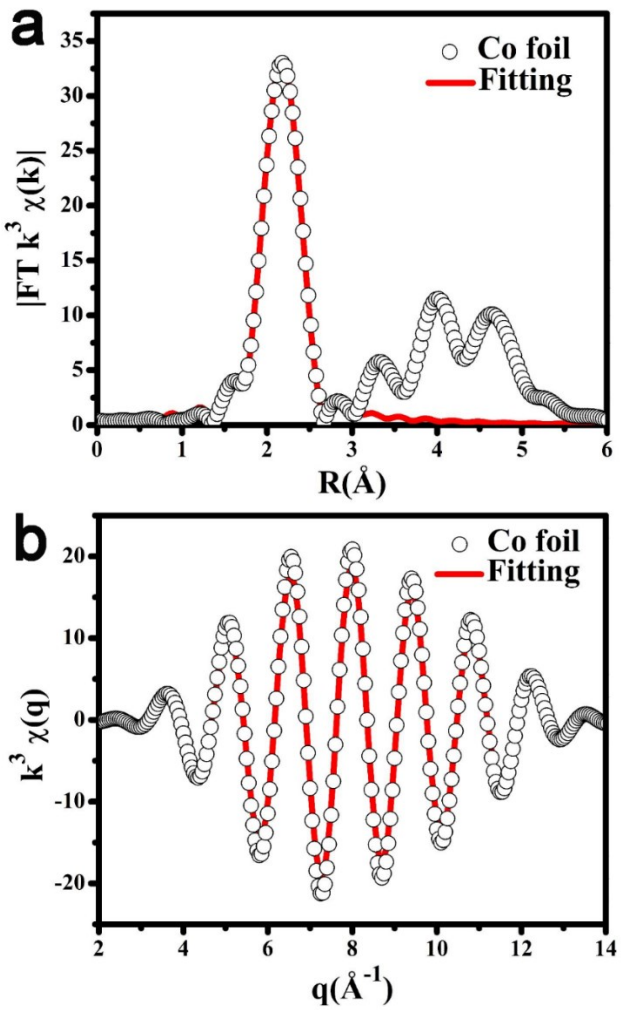

Fig. S22. (a) The FT-EXAFS fitting curves of Co foil at Co K-edge. (FT range: 2-11.8 $Å^{-1}$; fitting range: 1.4-2.7 Å). (b) The inversed FT-EXAFS fitting curves of Co foil at Co K-edge.

The bond length of each Co-N/P bonds were listed in Table. S4. Since P atoms are much larger then C or N atoms, it will lead to a significant shape distortion when P is doped in graphene. And the Co-N or Co-P bonds were lengthened (model 3, 4, 5, 6), which was consistent with the EXAFS results. For model 1 and model 2 (Co-N_4-C and Co NP@Co-N_4-C), the binding of Co-I was strong and the rate limiting step was the desorption of I^- (Fig. S20). When P was doped in the Carbon layer, it became positive charged (Table. S4), because the electronegativity of P is smaller than C. Therefore, P atom in Carbon was an electron donor, which decreased the Bader charge of Co (Table. S4). With the decreasing of Bader charge of Co, the electrostatic force between Co and I decreased and the adsorption of I weakened. Thus, P doping in the Carbon layer promote the desorption of I^-. However, if the adsorption of I was too weak, the rate limiting step would change, and hinder the reaction. Interestingly, the P atom inserted between the Carbon layer and metallic Co was negative charged (model 4 and 6). It could be used to regulate the electronic structure of Co. With the coordination of the two types of P atoms, the free energy change was only 0.004 eV in model 6. Notably, this result was reasonable under an assumption that there was a bias voltage ($U=E_0$) to balance the chemical potential of $2I^-$ and $I_2(g)+2e^-$, when the working electrode was catalyzing the reaction. The overpotentials measured under real experimental conditions may be under a different benchmark. However, qualitative conclusion could be made that the catalyzer with additional Co-P coordination promote the catalytic activity.

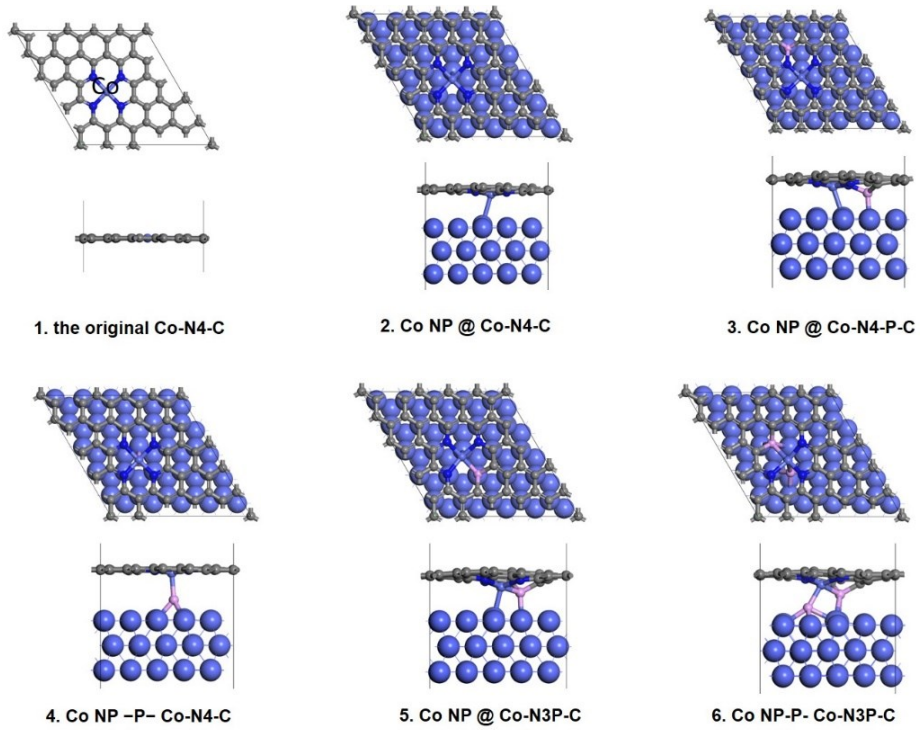

Fig. S23. DFT models for MODEL-1(the original Co-N_4-C), MODEL-2(Co NP@Co-N_4-C), MODEL-3(Co NP@Co-N_4-P-C), MODEL-4(Co NP-P-Co-N_4-C), MODEL-5(Co NP@Co-N_3P-C), MODEL-6 (Co NP-P-Co-N_3P-C).

Table. S1. Structural parameters extracted from the Co K-edge EXAFS fitting. (S_0^2=0.88)

Sample	Scattering pair	CN	R(Å)	$\sigma^2(10^{-3}Å^2)$	ΔE_0(eV)	R factor
$Co/Co_1P_1N_3$	Co-N	3.1	1.86	10.1	1.9	0.0014
	Co-P	1.1	2.18	10.9	-7.0	
	Co-Co	3.4	2.63	9.2	-0.9	
Co/Co_1N_4	Co-N	2.8	1.91	5.6	-2.5	0.0008
	Co-Co	2.4	2.50	6.2	-2.3	
Co foil	Co-Co	12*	2.49	6.3	6.1	0.0017

S_0^2 is the amplitude reduction factor; CN is the coordination number; R is interatomic distance (the bond length between Co central atoms and surrounding coordination atoms); σ^2 is Debye-Waller factor (a measure of thermal and static disorder in absorber-scatterer distances); ΔE_0 is edge-energy shift (the difference between the zero kinetic energy value of the sample and that of the theoretical model). R factor is used to value the goodness of the fitting. * This value was fixed during EXAFS fitting, based on the known structure of Co metal, CoP and Co_2N bulk.

Error bounds that characterize the structural parameters obtained by EXAFS spectroscopy were estimated as N ± 20%; R ± 1%; σ^2 ± 20%; ΔE_0 ± 20%.

Table. S2. Photovoltaic performance using different CEs

	J_{SC} (mA/cm^2)	V_{OC} (V)	*PCE* (%)	*FF* (%)
Conventional Pt	15.62	0.725	7.88	69.58
$Co/Co_1P_1N_3$	16.53	0.725	8.51	71.01
Co/Co_1N_4	13.07	0.720	6.62	70.03
PNC	11.73	0.710	5.83	70.00
NC	10.82	0.710	5.23	68.08

Table. S3. Electrochemical properties of different CEs

	J_{Red-1} (mA/cm^2)	*Epp* (V)	*Rct* (Ω cm^2)
Conventional Pt	2.23	0.236	5.92
$Co/Co_1P_1N_3$	2.35	0.157	5.39
Co/Co_1N_4	2.05	0.325	14.89
PNC	1.81	0.463	32.37
NC	1.77	0.559	43.23

Table. S4. Bond length, Bader charge, adsorption energy and overpotential of each model.

	Model	1	2	3	4	5	6
Bond length (Å)	Co-N1	1.88	1.89	1.84	1.90	1.96	1.96
	Co-N2	1.88	1.90	1.90	1.90	1.89	1.91
	Co-N3	1.88	1.91	1.88	1.90	2.00	2.00
	Co-N4/P	1.88	1.91	1.98	1.90	2.09	2.16
Bader Charge (e)	Co	+1.06	+0.93	+0.92	+0.99	+0.75	+0.81
	N1	-2.55	-2.58	-2.54	-2.54	-2.59	-2.59
	N2	-2.57	-2.60	-2.60	-2.57	-2.62	-2.62
	N3	-2.55	-2.58	-2.62	-2.57	-2.56	-2.60
	N4/P	-2.52	-2.55	-2.57	-2.55	+2.21	+2.15
	P2	\	\	\	-0.34	\	-0.40
Ead(eV)	*I	-0.82	-0.51	-0.28	-0.09	-0.20	-0.25
G(eV)	*I	-0.56	-0.25	-0.02	0.16	0.05	0.004
η-0.54 (V vs. SHE)		0.56	0.25	0.02	0.16	0.05	0.004

The structure of CoN_4 is very orderly, but the difference between the radius of P atom and N atom is large after adding P atom, which leads to the distortion of chemical bond between surrounding atoms and the lengthening of bond length.

The electronegativity of P is less than that of C and N, so P gives electrons in the graphite layer, which is positively charged. The positive charge of Co becomes weaker and the negative charge of N is more negative.

Table. S5. The comparison of IRR performance of nonnoble-metal counter electrodes in other works.

Sample	PCE	Author	Year	Reference
TiN, TaN	7.73%	X. P. Gao et al.	2009	Chem. Commun.,2009, 6720-6722.
Carbon	7.5%	Tingli Ma et al.	2011	Energy Environ. Sci., 2011, 4, 2308-2315.
MoC	8.34%	Tingli Ma et al.	2011	Angew. Chem. Int. Ed. 2011, 50, 3520-3524.
FeS_2, CoS, MoS	7.31%; 6.5%	Chun-Wei Chen Mingkui Wang et al.	2013	Angew. Chem. Int. Ed. 2013, 52, 6694-6698.
Co-Ni alloys	8.39% $CoNi_{0.25}$	Liangmin Yu et al.	2014	Angew. Chem. Int. Ed. 2014, 53, 10799-10803.
Ni-Fe alloys	8.82%	Wen-Hua Zhang et al.	2014	Angew. Chem. Int. Ed. 2014, 53, 7023-7027.
Co-C	8.4%	Dehui Deng et al.	2016	Angew. Chem. Int. Ed. 2016, 55, 1-6.

References

1. P. E. Blochl, Projector augmented-wave method, Phys. Rev. B: Condens. *Matter Mater. Phys.*, 1994, **50**, 17953.

2. G. Kresse and J. Hafner, Ab-initio molecular-dynamics for open-shell transition-metals, Phys. Rev. B: Condens. *Matter Mater. Phys.*, 1993, **48**, 13115−13118.

3. G. Kresse and J. Hafner, Ab-initio molecular-dynamics simulation of the liquid-metal amorphous-semiconductor transition in germanium, Phys. Rev. B: Condens. *Matter Mater. Phys.*, 1994, **49**, 14251−14269.

4. G. Kresse and J. Furthmüller, Efficiency of ab-initio total energy calculations for metals and semiconductors using a plane-wave basis set, *Comput. Mater. Sci.*, 1996, **6**, 15−50.

5. G. Kresse and J. Furthmüller, Efficient iterative schemes for ab initio total-energy calculations using a plane-wave basis set, *Phys. Rev. B: Condens. Matter Mater. Phys.*, 1996, **54**, 11169.

6. J. P. Perdew, K. Burke and M. Ernzerhof, Generalized Gradient approximation made simple, *Phys. Rev. Lett.,* 1996, **77**, 3865−3868.

7. J. Ran, T. Y. Ma, G. Gao, X. W. Du and S. Z. Qiao, Porous P-doped graphitic carbon nitride nanosheets for synergistically enhanced visible-light photocatalytic H_2 production, *Energy Environ. Sci.*, 2015, **8**, 3708-3717.

8. H. Gu, Y. Gu, Z. Li, Y. Ying and Y. Qiao, Low-temperature route to nanoscale P_3N_5 hollow spheres, *J. Mater. Res.,* 2003, **18**, 2359-2363.

9. S. Liu, H. Zhu, W. Yao, K. Chen and D. Chen, One step synthesis of P-doped g-C_3N_4 with the enhanced visible light photocatalytic activity, *Appl. Surf. Sci.,* 2018, **430**, 309-315.

10. L. L. Cao, Q. Q. Luo, W. Liu, Y. Lin, X. K. Liu, Y. J. Cao, W. Zhang, Y. E. Wu, J. L. Yang, T. Yao and S. Q. Wei, Identification of single-atom active sites in carbon-based cobalt catalysts during electrocatalytic hydrogen evolution, *Nat. Catal*. 2019, **2**, 134-141.

11. B. Ravel and M. Newville, ATHENA and ARTEMIS: interactive graphical data analysis using IFEFFIT, *Phys. Scr.*, 2005, **115**, 1007-1010.